Seismic Fragility Analysis of Deteriorating Reinforced Concrete Buildings from a Life-Cycle Perspective

Kenneth Otárola
Graduate Student, Dept. of Science, Technology, and Society, Scuola Universitaria Superiore (IUSS) Pavia, Pavia, Italy

Leandro Iannacone
Research Fellow, Dept. of Civil, Environmental, and Geomatic Engineering, University College London, London, United Kingdom

Roberto Gentile
Lecturer (Assistant Professor), Institute for Risk and Disaster Reduction, University College London, London, United Kingdom

Carmine Galasso
Professor (Full), Dept. of Civil, Environmental, and Geomatic Engineering, University College London, London, United Kingdom

ABSTRACT: Structural systems in seismically-active regions typically undergo multiple ground-motion sequences during their service life (including multiple mainshocks, mainshocks triggering other earthquakes on nearby fault segments, mainshock-aftershock, and aftershock-aftershock sequences). These successive ground motions can lead to severe structural/non-structural damage and significant direct/indirect earthquake-induced losses. Nevertheless, the effects of a pre-damaged state during ground-motion sequences are often neglected in assessing structural performance. Additionally, environmentally-induced deterioration mechanisms may exacerbate the consequences of such ground-motion sequences during the structural system's designed lifetime. Yet, such combined effects are commonly overlooked. This paper proposes an end-to-end computational methodology to derive time- and state-dependent fragility relationships (i.e., explicitly depending on time and the damage state achieved by a system during a first shock) for structural systems subjected to chloride-induced corrosion deterioration and earthquake-induced ground-motion sequences. To this aim, a vector-valued probabilistic seismic demand model is developed. Such a model relates the dissipated hysteretic energy in the ground-motion sequence to the maximum inter-storey drift induced by the first shock and the intensity measure of the second shock for a given corrosion deterioration level. Moreover, a vector-valued generalised logistic model is developed to estimate the probability of collapse, conditioning on the same parameters as above. An appropriate chloride-penetration model is then used to model the time-varying evolution of fragility relationships' parameters using a plain Monte-Carlo approach, capturing the continuous nature of the deterioration processes (i.e., gradual and shock deterioration). The significant impact of such a multi-hazard threat on structural fragility is demonstrated by utilising a case-study reinforced concrete building. Due to deteriorating effects, reductions up to 33.3% can be noticed in the fragility median values.

1. INTRODUCTION

The satisfactory structural and/or non-structural performance (e.g., their safety) of buildings is vital to ensure an adequate recovery after significant disastrous events (i.e., their resilience), such as significant earthquake-induced ground shaking. Thereby, buildings must not sustain significant damage after major earthquake events

during their service life. Current procedures to assess buildings' structural performance rely on several nonlinear dynamic analyses, each considering a single seismic excitation. The analysis results are then statistically processed to derive the distribution of structural response and resulting damage/loss estimates. Nevertheless, a building located in a seismically active region typically undergoes a series of multiple ground-motion sequences throughout its designed lifetime (e.g., consecutive mainshocks, a mainshock triggering additional earthquakes on nearby fault segments, mainshock-aftershock and aftershock-aftershock sequences). Therefore, such structures can often be in a pre-damaged state due to previous ground motion(s) when undergoing a seismic excitation. These series of back-to-back ground motions can lead to severe structural/non-structural damage and significant direct/indirect earthquake-induced losses. In addition, a substantial percentage of buildings across the globe show visible signs of ageing and material deterioration (e.g., Dizaj et al., 2022), particularly apparent when they approach the end of their service life. In this regard, deteriorating effects (e.g., steel rebar corrosion) constitute an environmentally-induced mechanism of gradual damage accumulation (e.g., Otárola et al., 2022) that exacerbates the consequences associated with ground-motion sequences. Therefore, in seismic-prone regions, the simultaneous consideration of infrequent earthquake-induced ground-motion sequences together with environmentally-induced deterioration is critical for risk-informed decision-making on potential mitigation strategies for vulnerable buildings. To address this issue, a methodology to derive time- and state-dependent fragility relationships for deteriorating buildings subject to ground-motion sequences is herein introduced, enabling the account of a building's structural performance in a life-cycle perspective.

2. METHODOLOGY

This study proposes an end-to-end computational methodology to derive time- and state-dependent fragility relationships for deteriorating reinforced concrete (RC) buildings under seismic sequences.

A procedure to select ground-motion record pairs (representing generic ground-motion sequences) exhibiting a wide range of earthquake-induced ground-motion intensity measures (IMs) is first introduced. The average pseudo-spectral acceleration is herein adopted as an IM ($avgSA$; geometric mean the pseudo-spectral acceleration in a range of structural periods of interest). Subsequently, both a vector-valued probabilistic seismic demand model (PSDM) and a collapse generalised logistic model (CGLM) are developed for estimating the probability of exceedance of a damage state (DS) given no collapse (NC) and the probability of collapse (C), respectively. The total probability theorem is then used to derive state-dependent fragility relationships as a function of a selected deterioration parameter. An appropriate chloride-penetration model (i.e., Duracrete, 2000) is finally used to transform the state-dependent fragility relationships into both time- and state-dependent fragility relationships. Namely, the stochastic evolution of the deterioration parameter (given by Duracrete, 2000) is used to sample the fragility median values as a function of time through a plain Monte-Carlo approach. The Probability Density Function (PDF) of the fragility median values is then modelled using a time-varying gamma-inflated distribution.

2.1. Case-Study Definition

The proposed methodology is demonstrated by analysing an archetype case-study RC moment-resisting frame (Figure 1), representing a typical building class in Southern Italy (e.g., Minas & Galasso, 2019). Such a case-study frame is characterised by a total height equal to 13.5 m (i.e., a first story of 4.5 m and upper stories of 3.0 m) and a total length equal to 18.0 m (i.e., bay spans of 4.5 m). It includes beams and columns with 30x50 cm cross sections, designed and detailed according to Eurocode 8 Part 3 (EC8-3) seismic provisions for high ductility class structures (EN 1998-3, 2005). The frame's structural response is simulated using a Finite Element Model (FEM) developed in OpenSeesPy (Zhu et al., 2018). Such a model captures the two-dimensional structural behaviour, and it accounts

for the geometry, the boundary conditions, the mass distribution, the energy dissipation, and the interactions among the structural components (based on the assumption that the building is regular and symmetric). The gravity loads are uniformly distributed on the beams, and the masses are concentrated at each storey beam-column nodes. Elastic damping is modelled through the Rayleigh model (Zareian & Medina, 2010), using a 5.0% viscous damping ratio on the first two structural vibration modes. Geometric nonlinearities are incorporated to account for destabilising $P - \Delta$ effects. Beams and columns are modelled with fibre-discretised cross-sections (including their shear behaviour), lumping the plasticity at two plastic hinges located at the opposite ends of the components, connected by a linear elastic element. The beam-column end-offsets are modelled as rigid.
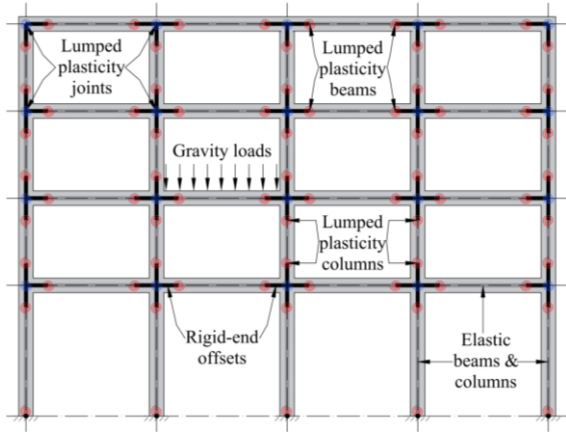

Figure 1: Geometric layout and nonlinear modelling strategy of the case-study frame

2.2. Ground-Motion Sequences

The ground-motion sequences (i.e., a first ground motion G1 followed by a second ground motion G2) are obtained using the simulated annealing method (i.e., dual annealing; e.g., Kirkpatrick et al., 1983) described in Iacoletti et al. (2023). Such a method allows the selection of ground-motion record pairs with IM values ($avgSA_{G1}$ and $avgSA_{G2}$) nearly following a discrete uniform distribution, covering a wide range of values of interest. This selection is consistent with the adopted nonlinear analysis procedure (i.e., cloud

analysis). To guarantee statistical independence of the data points used for fitting the PSDM and CGLM models, a set of constraints are imposed on the unscaled G1 and G2 records used to assemble the ground-motion sequences: 1) records scaling factor must be strictly in the range [0.5, 2.0], so that G1 and G2 are moderately scaled (Dávalos & Miranda, 2019); 2) each record pair (G1-G2) can only be selected once; 3) at least 70% of the selected records associated with a G1 or G2 must be unique (Iacoletti et al., 2023); 4) each record pair cannot comprise horizontal components of same recorded ground motion (Jalayer et al., 2017). By selecting $avgSA$ as the conditioning IM, the outcome of the fragility analysis is less sensitive to seismological features and ground-motion characteristics (e.g., spectral shape), as shown in Kohrangi et al., (2017). Figure 2 presents the $avgSA_{G1}$ and $avgSA_{G2}$ for the 400 selected ground-motion record pairs, along with the corresponding marginal histograms.
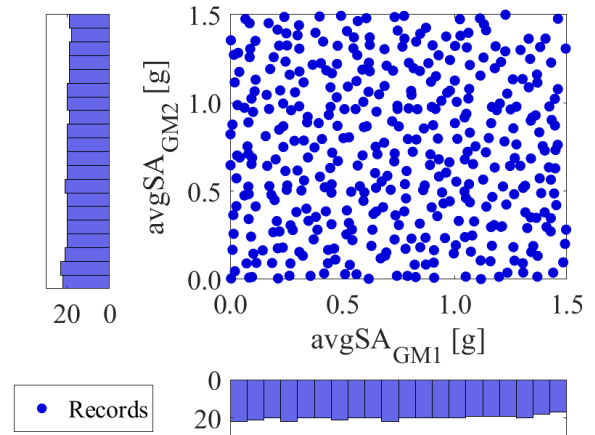

Figure 2: Ground-motion $avgSA_{G1}$ vs $avgSA_{G2}$ selection and marginal histograms

2.3. Corrosion-Induced Deterioration

Chloride-induced corrosion of rebars is one of the most significant environmental threats affecting the structural performance of buildings worldwide (e.g., Claisse, 2008). Once the corrosion process initiates, a series of primary and secondary effects can be observed in the affected RC components due to the extensive build-up of rust products. The primary effects are associated with the direct deterioration in the rebar (i.e., the loss of cross-

sectional area), while the secondary effects are related to the indirect deterioration of the rebar and concrete properties (e.g., reduction of the materials' ultimate strength/strain). In general, chloride-induced corrosion eventually results in wide interconnected cracks in the rebars leading to uniform (also known as generalised) corrosion, as observed in section A-A in Figure 3. However, in addition to the uniform area loss, more severe, localised corrosion across multiple locations along the rebars can lead to deep-pit formations (i.e., a pitting sectional area loss). Experimental investigations have reported that these cavities are often four to eight times deeper than the ones attained under uniform corrosion (e.g., Hanjari et al., 2011). Therefore, uniform corrosion models assume a consistent loss of area around the circumference of the rebar during the building's designed lifetime. In contrast, pitting corrosion models assume an additional hemispherical area loss accompanying the loss due to uniform corrosion (e.g., Stewart, 2004), as observed in Section B-B in Figure 3. Further details on how to model corrosion-induced deterioration can be found in Otárola et al. (2022).
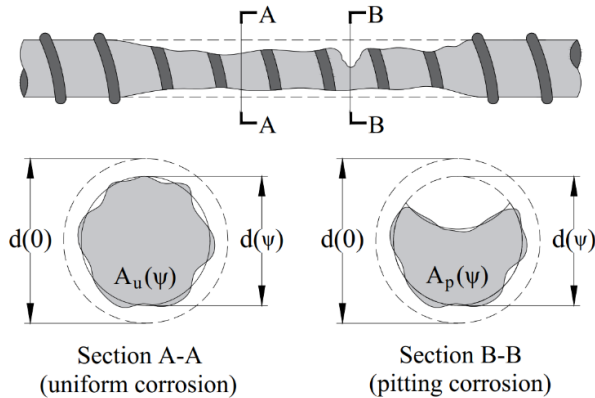

Figure 3: Uniform and pitting corrosion on a single steel rebar scheme

Before obtaining time- and state-dependent fragility relationships including corrosion, state-dependent (only) relationships are first obtained as a function of a given deterioration parameter ψ quantifying the corrosion deterioration level. The adopted ψ corresponds to rebar diameter loss, as obtained from a corrosion-penetration model.

Additional details on the physical interpretation of ψ can also be found in Otárola et al. (2022). In total, ten equally-spaced ψ values are considered to perform the fragility analysis of the case-study frame, ranging from ψ =0.0 mm (i.e., pristine condition) up to ψ=1.5 mm (a realistic value of ψ at the end of the service life of typical buildings; e.g., Du et al., 2005). The ψ is assumed to be constant across the building since its components are similarly exposed to chlorides.

2.4. Fragility Analysis
Sequential cloud nonlinear time-history analyses (NLTHAs) are conducted for the selected ground-motion sequences. From the results, the maximum inter-storey drift is obtained for G1, while the dissipated hysteretic energy is obtained for both ground motions within the sequence (i.e., the proportion of the dissipated hysteretic energy achieved during G1 and G2; i.e., $E_{H,G1}$ and $E_{H,G2}$, respectively). The described analysis is repeated for each value of ψ. State-dependent fragility relationships are derived using the PSDM and CGLM for four DSs, as shown in the subsequent subsections. Those DSs are defined by pushover analysis (using a load pattern defined according to EC8) as slight (DS1), moderate (DS2), severe (DS3), and complete (DS4); selected using the multiple measurable criteria shown in Otárola et al. (2023). Drift-based DS thresholds are also defined; they evolve with ψ according to an ordinary least-squares regression based on the obtained pushover results. More details on such a model can be found in Otárola et al. (2022).

2.4.1. PSDM model implementation
The developed vector-valued PSDM (Figure 4) relates the total dissipated hysteretic energy (E_H) during a seismic sequence to a maximum inter-storey drift induced by G1 (θ_{G1}) and an $avgSA$ related to G2 (IM_{G2}), calibrated by sequential cloud NLTHAs for different values of ψ (e.g., Gentile & Galasso, 2021; Otárola et al., 2022). A ten-parameter functional form is adopted, as shown in Equations (1) to (5). The standard deviation (σ_{E_H}) is computed as the root mean-squared error of the proposed model. The

sequential steps to fit the PSDM functional form are summarised as follows:

1. The $\widehat{E_{H,G1}} = a_0\theta_{G1}{}^{b_0}$ relationship is fitted using the data corresponding to G1 through linear ordinary least-squares regression in log space; the parameters a_0 and b_0 are obtained.

2. The $\widehat{E_{H,G1}} = c_0 IM_{G1}{}^{d_0}$ relationship is fitted using the data corresponding to G1 through linear ordinary least-squares regression in log space; the parameters c_0 and d_0 are obtained.

3. The $\widehat{E_{H,G2}} = c_0(1 - m_0\theta_{G1})IM_{G2}{}^{d_0}$ is fitted using the data corresponding to G1 and G2 through nonlinear least-squares regression in log space; the parameter m_0 is obtained.

4. The $\widehat{E_H} = a(\psi)\theta_{G1}{}^{b(\psi)} + c(\theta_{G1},\psi)IM_{G2}{}^{d(\psi)}$ relationship is fitted using the data related to G1, G2 and ψ through nonlinear least-squares regression in log space; the parameters a_1, b_1, c_1, d_1, and m_1 are obtained.

$$\mu_{E_H} = \widehat{E_H} = a(\psi)\theta_{G1}{}^{b(\psi)} + c(\theta_{G1},\psi)IM_{G2}{}^{d(\psi)} \quad (1)$$

$$a(\psi) = a_0 + a_1\psi \quad (2)$$

$$b(\psi) = b_0 + b_1\psi \quad (3)$$

$$c(\theta_{G1},\psi) = (c_0 + c_1\psi)[1 - (m_0 + m_1\psi)\theta_{G1}] \quad (4)$$
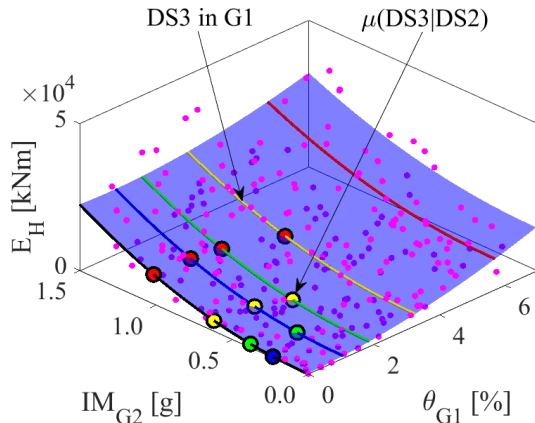
$$d(\psi) = d_0 + d_1\psi \quad (5)$$

Figure 4: Vector-valued PSDM of the case-study frame evaluated at $\psi = 0$ (Response: magenta dots)

The probability of exceedance a DS given NC can be estimated using Equation (6). $\overline{E_{H,\iota}}$ corresponds to an energy-based DS threshold

associated to the ith DS (ds) obtained directly from the PSDM, as a function of ψ. $\boldsymbol{\Theta}$ is a vector containing all the PSDM (and those for CGLM) conditioning parameters (i.e., $[DS_{G1}, IM_{G2}, \psi]$).

$$P(DS_{G2} > ds|\boldsymbol{\Theta}, NC) = 1 - \Phi\left[\frac{ln\left(\frac{\overline{E_{H,\iota}}}{\mu_{E_H}}\right)}{\sigma_{E_H}}\right] \quad (6)$$

2.4.2. CGLM model implementation

The developed vector-valued CGLM (Figure 5) also relates the E_H during the sequence to a θ_{G1} induced by G1 and an IM_{G2} related to G2 (as in the PSDM); as a function of ψ. Such a model is calibrated using the generalised logistic function formulation (e.g., Iacoletti et al., 2023; Richards, 1959). A six-parameter functional form is adopted, as shown in Equations (7) to (9). $\overline{\theta_C(\psi)}$ is the deformation-based DS threshold associated to structural collapse, and it is also a function of ψ. The proposed CGLM provides the probability of C (i.e., $P(C|\boldsymbol{\Theta})$). When the DS thresholds are deterministic, the $P(C|\boldsymbol{\Theta})$ in the $P(C|\boldsymbol{\Theta})$ - θ_{G1} space corresponds to a step function (Figure 5). The sequential steps to fit the CGLM functional form are summarised as follows:
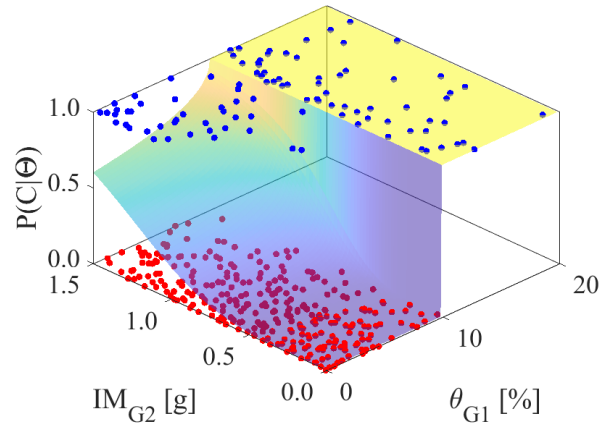

Figure 5: Vector-valued CGLM of the case-study frame evaluated at $\psi = 0$ (C: blue dots; NC: red dots)

1. The $P(C|\theta_{G1}, \psi) = \frac{1}{1 + e^{-[\alpha_0 + \alpha_1 ln(\theta_{G1}) + \alpha_2\psi]}}$ is calculated using the data corresponding to G1 through multiple logistic regression; the parameters α_0, α_1 and α_2 are obtained.

2. The $P(C|IM_{G1}, \psi) = \frac{1}{1+e^{-[\beta_0+\beta_1 ln(IM_{G1})+\beta_2\psi]}}$ is calculated using the data corresponding to G1 through multiple logistic regression; the parameters β_0, β_1 and β_2 are obtained.

$$P(C|\boldsymbol{\theta}) = A + (1-A)B \tag{7}$$

$$P(C|\theta_{G1}, \psi) = A = \frac{1}{1+e^{-[\alpha_0+\alpha_1 ln(\theta_{G1})+\alpha_2\psi]}} \tag{8}$$

$$P(C|\theta_{G1}, IM_{G2}, \psi) = B$$
$$= \frac{1}{1+\sqrt{1-\frac{\theta_{G1}}{\theta_C(\psi)}}e^{-[\beta_0+\beta_1 ln(IM_{G2})+\beta_2\psi]}} \tag{9}$$

2.4.3. State-dependent fragility

The total probability theorem is used to estimate the fragility relationships, combining the $P(C|\boldsymbol{\theta})$ and $P(DS_{G2} > ds|\boldsymbol{\theta}, NC)$, as shown in Equation (10). This estimates the conditional probability of exceeding a DS conditioned on $\boldsymbol{\theta}$. Figure 6 shows the seismic state-dependent fragility relationships for the case-study frame in pristine conditions.

$$P(DS_{G2} > ds|\boldsymbol{\theta}) =$$
$$P(C|\boldsymbol{\theta}) + [1 - P(C|\boldsymbol{\theta})]P(DS_{G2} > ds|\boldsymbol{\theta}, NC) \tag{10}$$
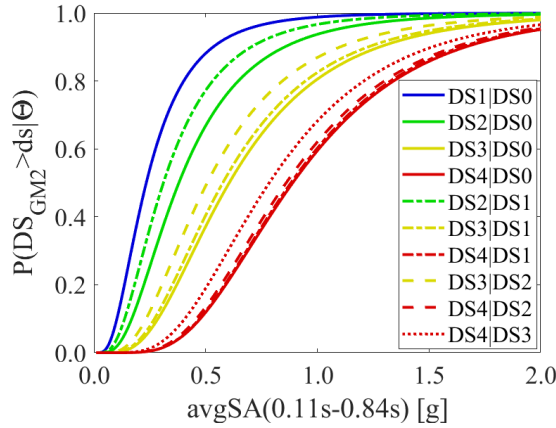

Figure 6: DS4 state-dependent fragility relationships for the case-study frame evaluated at $\psi = 0$

Figure 7 shows the fragility median values (i.e., $\mu(DS_{G2}|\boldsymbol{\theta})$) of each fragility relationship as a function of ψ. As expected, the median values of such relationships decrease with ψ (i.e., the relationships are shifted to the left). It is observed that deteriorating effects are more evident for

DS4, agreeing with previous observations (e.g., Otárola, Gentile, et al., 2023; Otárola, Sousa, et al., 2023), where damage accumulation on structural components is more apparent when they are close to their peak strength, after which strain-softening starts. Since E_H is used as an engineering demand parameter, damage accumulation can also be captured at lower DSs, as expected. As per the adopted modelling assumptions, the dispersion (i.e., $\beta(DS_{G2}|\boldsymbol{\theta})$) of the various fragility relationships is nearly constant; thus, it can be further assumed as a constant value by simply taking the mean of the linear model illustrated in Figure 7.
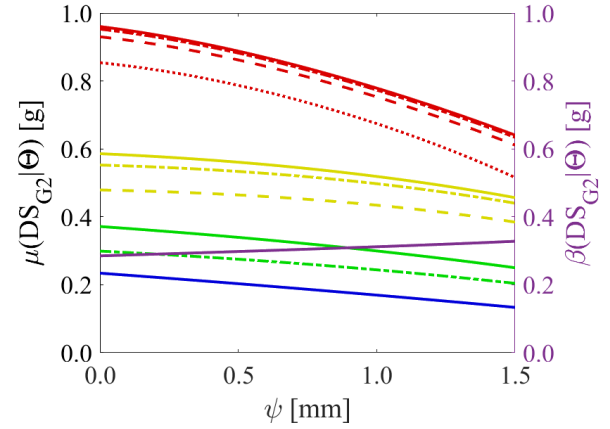

Figure 7: Evolution of the case-study frame's fragility median values and dispersion as a function of ψ

2.4.4. Time- and state-dependent fragility

Time- and state-dependent fragility relationships are obtained from the relationships (conditioned on ψ) obtained in the previous section. Time- and state-dependent fragilities can be used to perform life-cycle consequence analyses of the building (e.g., lifetime assessment of repair costs, downtime, and casualties; e.g., Otárola et al., 2023). To derive the time- and state-dependent fragility relationships, the DuraCrete (2000) chloride-penetration model is used to obtain the evolution of ψ over time. Then, the fragility median values are sampled from realisations of the corrosion rate evolution in time by plain Monte-Carlo simulation. According to DuraCrete (2000), chloride-induced corrosion starts at the corrosion initiation time T_i obtained from

Equation (11). In such an equation, c is the concrete cover depth, k_e is the environmental parameter, k_c is the execution parameter, k_t is the test method parameter, D_0 is the reference chloride diffusion coefficient, t_0 is the reference time at compliance test, n_d is the age factor, C_s is the equilibrium chloride concentration at the concrete surface, C_{cr} is the critical chloride concentration. Details regarding the PDF of each parameter can be found in Shekhar et al. (2018).

$$T_i = \left\{ \frac{c^2}{4k_e k_c k_t D_0 (t_0)^{n_d}} \left[erf^{-1} \left(\frac{C_s - C_{cr}}{C_s} \right) \right]^{-2} \right\}^{\frac{1}{(1-n_d)}} \quad (11)$$

The case-study frame is assumed to be located in a marine splash environment. Hence, the initial corrosion rate (r_0) is simulated from a uniform distribution with a mean equal to 3.1 $\mu A/cm^2$ and a standard deviation equal to 0.2 $\mu A/cm^2$. The corrosion rate evolution (r_c) in the time (t_p) after T_i is described in Equation (12). By concatenating the realisations for T_i and r_c, the corrosion rate is fully described as a function of time. The fragility median values (Figure 7) are then associated with such realisations through the corresponding ψ (related to a r_c value). Thus, the evolution of the fragility median values in time is also fully described, as shown in Figure 8.

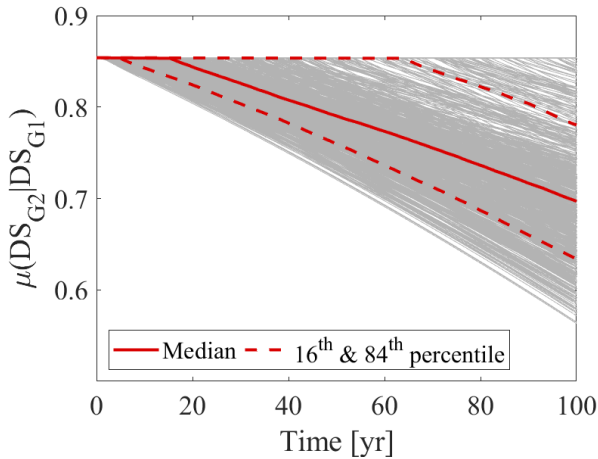$$r_c(t_p) = 0.0116(0.85 r_0 t_p^{-0.29}) \quad (12)$$

Figure 8: Evolution of the DS4|DS3 fragility median value as a function of time

A gamma-inflated model is then fitted to the realisations (Figure 8) of $\mu(DS_{G2}|\boldsymbol{\Theta})$ at time t. The PDF of the gamma-inflated model is given by Equation (13). The realisations at t, excluding those related to the $\mu(DS_{G2}|\boldsymbol{\Theta})$ maximum value (μ_{max}), are used to obtained the parameters (i.e., α and β) of the shown truncated gamma distribution $f_\Gamma(x|x < \mu_{max})$, where α is the shape parameter and β is the rate parameter (equal to the inverse of the scale parameter). The parameter p is simply computed as the probability of observing the μ_{max} among all the realisations at t. Estimates of the three parameters (i.e., α, β and p) are obtained for multiple values of t throughout the system's service life. Such estimates are illustrated as dots in Figure 9. Appropriate functional forms (e.g., exponential or polynomial) are then fitted to those estimates (also in Figure 9). The corresponding equations are not shown for brevity.

$$f(x)_t = \begin{cases} p + (1-p)f_\Gamma(x|x < \mu_{max}), & x = \mu_{max} \\ (1-p)f_\Gamma(x|x < \mu_{max}), & x \neq \mu_{max} \end{cases} \quad (13)$$
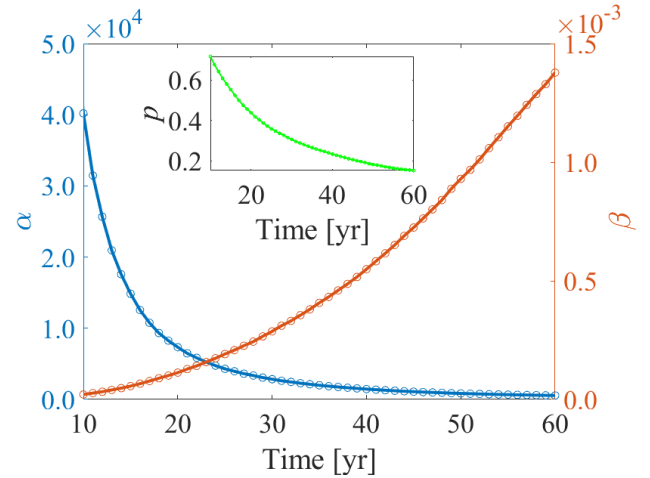

Figure 9: Evolution of the inflated-gamma model parameters as a function of time

3. CONCLUSIONS

This paper proposed an end-to-end computational framework for fragility analysis of deteriorating RC buildings under ground-motion sequences. A vector-valued probabilistic demand model and a collapse generalised logistic model are calibrated and utilised to derive time- and state-dependent

fragility relationships. The total dissipated hysteretic energy in the seismic sequence is adopted as the primary engineering demand parameter because it is a cumulative-based measure that monotonically increases with the length of the applied seismic excitation. Such a parameter allows the development of statistical models consistent with the physics of a building's structural system subject to seismic sequences, unlike peak-based parameters. The framework provides the means for assessing the seismic structural performance of RC buildings under individual ground motions or ground-motion sequences. The framework can also account for the impact of corrosion-induced deterioration (specifically, chloride-induced corrosion, but easily applicable to other types). The derived time- and state-dependent fragility relationships can be used, in general, for various locations since the selected intensity measure (i.e., $avgSA$) reduces the bias due to non-site-specific, non-hazard-consistent record selection. They can also be used for assessing a building's structural performance at a specific time or in a life-cycle analysis. The results can also be extended from a single building to a portfolio of buildings (for instance, through Monte-Carlo sampling).

4. ACKNOWLEDGEMENTS

5. REFERENCES

Afsar Dizaj, E., Salami, M. R., & Kashani, M. M. (2022). Seismic vulnerability assessment of ageing reinforced concrete structures under real mainshock-aftershock ground motions. *Structure and Infrastructure Engineering*, *18*(12). https://doi.org/10.1080/15732479.2021.1919148

Broomfield, J. P. (2006). Corrosion of Steel in Concrete: Understanding, Investigation and Repair, Second Edition. In *Broomfield J. P. , Taylor & Francis, London,* (Vols. 978-0–4153, Issues 3404–4). http://books.google.co.uk/books/about/Corrosion_of_Steel_in_Concrete.html?id=kjTzl9NVHsQC&pgis=1

Dávalos, H., & Miranda, E. (2019). Evaluation of the scaling factor bias influence on the probability of collapse using SA(T1) as the intensity measure. *Earthquake Spectra*, *35*(2). https://doi.org/10.1193/011018EQS007M

Du, Y. G., Clarkt, L. A., & Chan, A. H. C. (2005). Effect of corrosion on ductility of reinforcing bars. *Magazine of Concrete Research*, *57*(7). https://doi.org/10.1680/macr.2005.57.7.407

Duracrete. (2000). DuraCrete: Probabilistic Performance based Durability Design of Concrete Structures - Final Technical Report: General guidelines for durability design and redesign. In *Concrete*.

Eurocode 8. (2005). European Standard EN 1998-3:2005: Design of structures for earthquake resistance - Part 3: Assessment and retrofitting of buildings. *Comite Europeen de Normalisation, Brussels*, *3*(2005).

Gentile, R., & Galasso, C. (2021). Hysteretic energy-based state-dependent fragility for ground-motion sequences. *Earthquake Engineering & Structural Dynamics*, *50*(4), 1187–1203. https://doi.org/https://doi.org/10.1002/eqe.3387

Hanjari, K. Z., Kettil, P., & Lundgren, K. (2011). Analysis of mechanical behavior of corroded reinforced concrete structures. *ACI Structural Journal*, *108*(5). https://doi.org/10.14359/51683210

Iacoletti, S., Cremen, G., & Galasso, C. (2023). Modeling damage accumulation during ground-motion sequences for portfolio seismic loss assessments. *Soil Dynamics and Earthquake Engineering*, *168*, 107821. https://doi.org/https://doi.org/10.1016/j.soildyn.2023.107821

Jalayer, F., Ebrahimian, H., Miano, A., Manfredi, G., & Sezen, H. (2017). Analytical fragility assessment using unscaled ground motion records. *Earthquake Engineering and Structural Dynamics*, *46*(15). https://doi.org/10.1002/eqe.2922

Kirkpatrick, S., Gelatt, C. D., & Vecchi, M. P. (1983). Optimization by simulated annealing. *Science*, *220*(4598), 671–680. https://doi.org/10.1126/science.220.4598.671

Kohrangi, M., Vamvatsikos, D., & Bazzurro, P. (2017). Site dependence and record selection schemes for building fragility and regional loss assessment. *Earthquake Engineering and Structural Dynamics*, *46*(10).

https://doi.org/10.1002/eqe.2873

Minas, S., & Galasso, C. (2019). Accounting for spectral shape in simplified fragility analysis of case-study reinforced concrete frames. *Soil Dynamics and Earthquake Engineering*, *119*. https://doi.org/10.1016/j.soildyn.2018.12.025

Otárola, K., Fayaz, J., & Galasso, C. (2022). Fragility and vulnerability analysis of deteriorating ordinary bridges using simulated ground-motion sequences. *Earthquake Engineering and Structural Dynamics (in Press)*.

Otárola, K., Gentile, R., Sousa, L., & Galasso, C. (2023). Impact of earthquake-induced ground-motion duration on nonlinear structural performance. Part I: spectrally equivalent records and inelastic single-degree-of-freedom systems. *Earthquake Spectra (in Press)*.

Otárola, K., Iannacone, L., Gentile, R., & Galasso, C. (2023). A Markovian framework for multi-hazard life-cycle consequence analysis of deteriorating structural systems. *14th International Conference on Applications of Statistics and Probability in Civil Engineering, ICASP14*.

Otárola, K., Sousa, L., Gentile, R., & Galasso, C. (2023). Impact of earthquake-induced ground-motion duration on nonlinear structural performance. Part II: site- and building-specific analysis. *Earthquake Spectra (in Press)*.

Richards, F. J. (1959). A flexible growth function for empirical use. *Journal of Experimental Botany*, *10*(2). https://doi.org/10.1093/jxb/10.2.290

Shekhar, S., Ghosh, J., & Padgett, J. E. (2018). Seismic life-cycle cost analysis of ageing highway bridges under chloride exposure conditions: modelling and recommendations. *Structure and Infrastructure Engineering*, *14*(7). https://doi.org/10.1080/15732479.2018.1437639

Stewart, M. G. (2004). Spatial variability of pitting corrosion and its influence on structural fragility and reliability of RC beams in flexure. *Structural Safety*, *26*(4). https://doi.org/10.1016/j.strusafe.2004.03.002

Zareian, F., & Medina, R. A. (2010). A practical method for proper modeling of structural damping in inelastic plane structural systems. *Computers and Structures*, *88*(1–2), 45–53. https://doi.org/10.1016/j.compstruc.2009.08.001

Zhu, M., McKenna, F., & Scott, M. H. (2018). OpenSeesPy: Python library for the OpenSees finite element framework. *SoftwareX*, *7*.

https://doi.org/10.1016/j.softx.2017.10.009